Journal of the European Ceramic Society 42 (2022) 1292–1301

Contents lists available at ScienceDirect

Journal of the European Ceramic Society

journal homepage: www.elsevier.com/locate/jeurceramsoc

Fabrication and characterisation of single-phase $Hf_2Al_4C_5$ ceramics

Doni Daniel Jayaseelan [a,*], S. Pramana [b], S. Grasso [c,d], Y. Bai [c,d], S. Skinner [e], M.J. Reece [c], W. E. Lee [e]

[a] Department of Aerospace and Aircraft Engineering, Kingston University, London, SW15 3DW, UK
[b] Chemical Engineering in the School of Engineering at Newcastle University, UK
[c] Queen Mary University of London, UK
[d] Department of Materials Science, Southwest Jiaotong University, China
[e] Dept of Materials, Imperial College, London, SW7 2AZ, UK

ARTICLE INFO

Keywords:
Ternary carbides
$Hf_2Al_4C_5$
HRTEM
Microstructure
Oxidation
Thermal conductivity

ABSTRACT

Single-phase $Hf_2Al_4C_5$ ternary carbide was fabricated from Hf/Al/C powder mixtures by pressure assisted sintering techniques such as hot pressing and spark plasma sintering at 1900 °C for 3 h and 10 min, respectively. XRD confirmed that the ternary carbide started to form at temperatures as low as 1500 °C and with total formation of $Hf_2Al_4C_5$ after reactive sintering for 1 h at 1900 °C. It is evident from HRTEM that two Hf-C layers were sandwiched with 4 Al-C layers (Al_4C_3) in the $Hf_2Al_4C_5$ ternary carbide. Tight interlocking of grains, faceted grains and stacking faults were occasionally observed. Thermal conductivity of $Hf_2Al_4C_5$ is measured to be 14 w $m^{-1}k^{-1}$ from room temperature to 1300 °C. The oxidation studies carried out at 1300 °C for 3 h reveal that the oxidation layer thickness is around 220 μm and it contains microcracks closer to sample surface whereas the interface looks seamless without any cracking or spallation of the oxide layer.

1. Introduction

Transition metal carbides (TMCs), such as ZrC, HfC, TaC, and TiC display high melting point, high hardness, good wear resistance and chemical inertness, excellent thermal and electrical conductivities, thermal shock resistance, high reliability and machinability and absence of polymorphic transformations [1–8]. These properties make TMCs promising for applications in extreme environments such as in re-entry vehicles, rocket/scramjet engines, thermal protection systems for hypersonic vehicles, and structural and fuel cladding materials in Generation IV nuclear reactors [3,8–10]. However, intrinsic brittleness and poor oxidation resistance may cause TMCs to have low reliability. Inspired by the studies of MAX phases (which have general formula $M_{n+1}AX_n$, where M is an early transition metal, A is an A group element, X is either C and/or N {n = 1, 2, 3,. .}), we believe that incorporating Al into the binary carbides might significantly improve the ductility and oxidation resistance [11–19]. For example, Ti_3AlC_2, Ti_2AlC, and Cr_2AlC are MAX phases, which exhibit excellent oxidation resistance and damage tolerance along with the other benefits shared by other MAX phases outlined above.

Wang and Zhou [11] compiled recent progress in theoretical prediction, preparation and characterization of layered ternary transition metal carbides. Their review reveals that it is difficult to synthesize single-phase ternary carbides in Zr-Al-C and Hf-Al-C systems. Recently, a new family of layered ternary and quaternary compounds with the general formula of $(TC)_nAl_3C_2$ and $(TC)_n[Al(Si)]_4C_3$ (where T = Zr or Hf, n = 1, 2, 3.. .) was developed in Zr-Al(Si)-C and Hf-Al(Si)-C systems [20–24]. The high degree of stiffness retained at elevated temperatures make Zr-Al(Si)-C compounds promising candidates for applications in high temperature and ultra high temperature environments [24]. Michalenko et al. [25] and Nowotny et al. [26] have investigated complex carbides in the ternary Hf–Al–C system; two ternary carbides ($Hf_3Al_3C_5$ and $Hf_2Al_3C_4$) were discovered and determined to have hexagonal symmetry with space group P63/mmc. Their crystal structures can be described as Hf–C slabs in an NaCl-type structure intercalated by Al_3C_2 blocks, which is similar to the structure of the Zr–Al–C system [11–13]. Later, He et al. [24], successfully synthesized a Hf-Al-C composite composed of $Hf_3Al_3C_5$, $Hf_2Al_4C_5$ and $Hf_3Al_4C_6$ by a hot pressing method and investigated the effect of microstructure on mechanical and thermal properties. The composite exhibited much higher strength and fracture toughness than HfC due to its fine and anisotropic grains. The similarity in crystal structures for Zr–Al–C and Hf–Al–C suggests they

* Corresponding author.
E-mail address: d.daniel@kingston.ac.uk (D.D. Jayaseelan).

https://doi.org/10.1016/j.jeurceramsoc.2021.12.035
Received 15 September 2021; Received in revised form 2 December 2021; Accepted 12 December 2021
Available online 16 December 2021

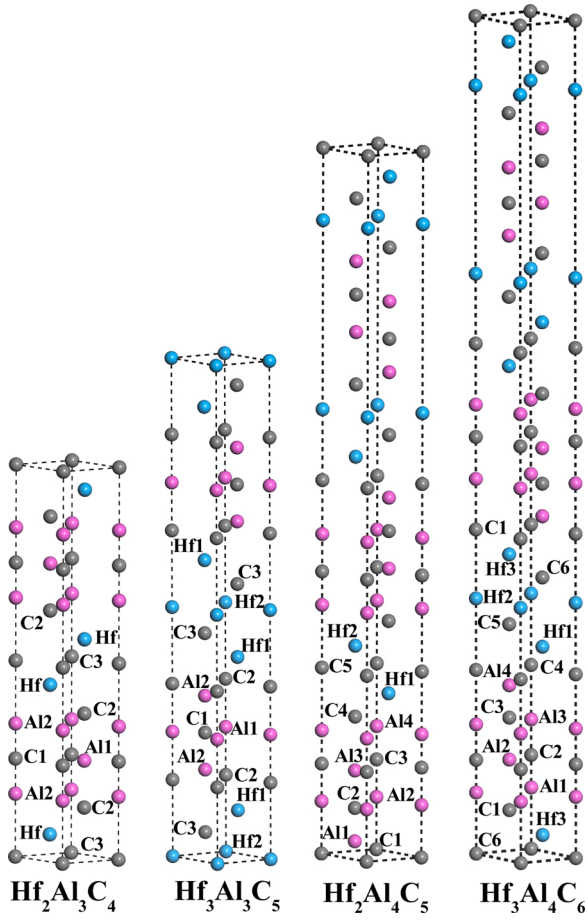

Fig. 1. Crystal structures of $Hf_2Al_3C_4$, $Hf_3Al_3C_5$, $Hf_2Al_4C_5$, and $Hf_3Al_4C_6$.

may have analogous elastic properties. In 2017, K.Song et al., successfully synthesized a layered ternary carbide phase, $Hf_2Al_4C_5$ by spark plasma sintering method and investigated a detailed (atomic-scale) microstructure of the ternary carbide [27]. A thorough study on the formation of $Hf_2Al_4C_5$ grains was carried out using microscopic techniques, in particular a clear analysis on the formation of stacking faults and its mechanism has been carried out [27]. However, the study does not have enough formation whether the desired phase was wholly formed after sintering.

All these previous reports inspired the motivation of fabricating single-phase ternary carbides in the Hf-Al-C system. In Hf-Al-C systems, a new class of layered ternary transition-metal carbides with the general formula $(MC)_nAl_3C_2$ and $(MC)_nAl_4C_3$ (where M = Hf, n = 1, 2, 3.. .) was identified in experiments [21]. They crystallise in the space group of R3m. The crystal structures can be regarded as intergrowth structures where the Al_4C_3-type (Al_3C_3 for $(MC)_nAl_3C_2$ or Al_4C_4 for $(MC)_nAl_4C_3$) layers in the Al-C slabs are the same, while the NaCl-type (M_nC_{n+1}) layers increase in the M-C slabs with increasing n value. Each unit cell consists of two formulas for $(MC)_nAl_3C_2$, and three for $(MC)_nAl_4C_3$), respectively. The crystal structures of $Hf_2Al_3C_4$, $Hf_3Al_3C_5$, $Hf_2Al_4C_5$ and $Hf_3Al_4C_6$ are displayed in Fig. 1. As the information on the crystal structure and properties are limited due to the difficulty in synthesizing it in bulk form, a systematic investigation of the influences of different parameters such as sintering atmosphere, starting mixtures as well as the ratios of starting composition on the high purity of the $Hf_2Al_4C_5$ powder is necessary. To clarify why other Hf/Al/C compounds are always present, an understanding of the formation mechanism of $Hf_2Al_4C_5$ is always needed.

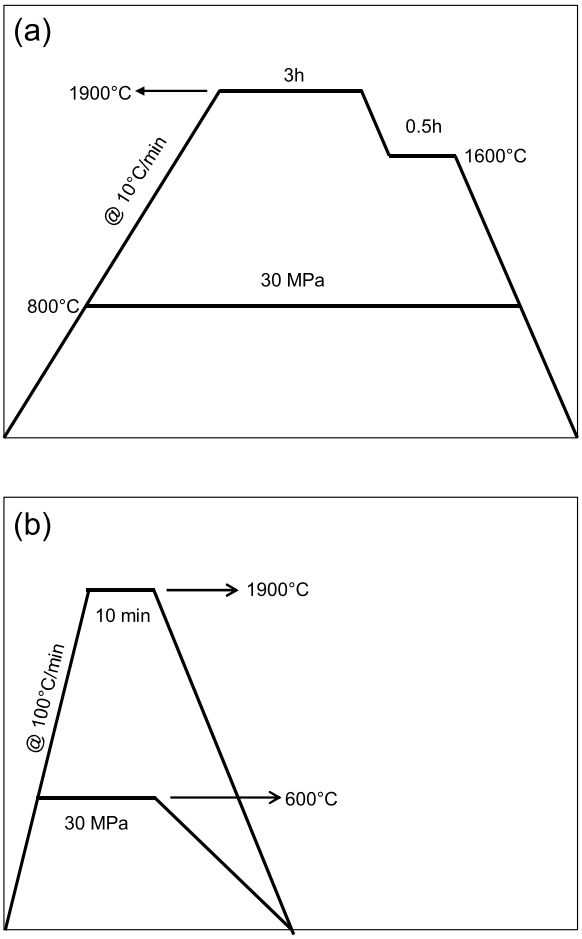

Fig. 2. Temperature profiles of HP and SPS experiments.

2. Experimental details

$Hf_2Al_4C_5$ ternary carbides in the Hf-Al-C system were prepared by an *in-situ* reactive sintering technique using elemental hafnium (99.9 %, 325 mesh, ABCR, Karlsruhe, Germany), aluminium (99.9 %, 325 mesh, ABCR, Karlsruhe, Germany) and graphite flakes (45 μm, ABCR, Karlsruhe, Germany) as the starting materials. Powder mixtures of Hf:Al:C = 2.0:4.15:5.1 for $Hf_2Al_4C_5$ composition were carefully weighed and sealed in a Teflon coated steel container. The non-stoichiometric ratio was chosen to compensate the loss of Al. The container was placed in an attrition mill and the powder mixtures were dry milled for 12 h. The dry milled powder mixtures were poured into a carbon foil lined graphite crucible of diameter 30 mm and uniaxially pressed at 20 MPa. All these steps were carried out inside a glove box to avoid oxygen contamination during powder processing. The mixed powders were reactively sintered by two different pressure assisted sintering techniques: (i) hot pressing (RHP) and (ii) spark plasma sintering (SPS). Reactive hot pressing (RHP) was carried out for 3 h at 1900 °C with an applied load of 30 MPa. Reactive spark plasma sintering (RSPS) was for 20 min at 1900 °C with an applied load of 30 MPa. The heating profiles of HP and SPS are shown in Fig. 2(a) and (b) respectively. Powder composition, synthesis temperature, atmosphere and powder purity play a vital role in preparing single-phase $Hf_2Al_4C_5$ ceramics. $Hf_2Al_4C_5$ phase was always synthesized by sintering a non-stoichiometric composition of Hf/Al/C in vacuum. Firstly, an Hf-Al-C mix was sintered in an SPS furnace. An exothermic reaction was expected during reactive sintering of metallic powders and also considering the high heating rate involved in SPS, the applied pressure was kept as low as possible [24]. In all SPS experiments, the pressure was only 20 MPa and it was the minimum pressure that could

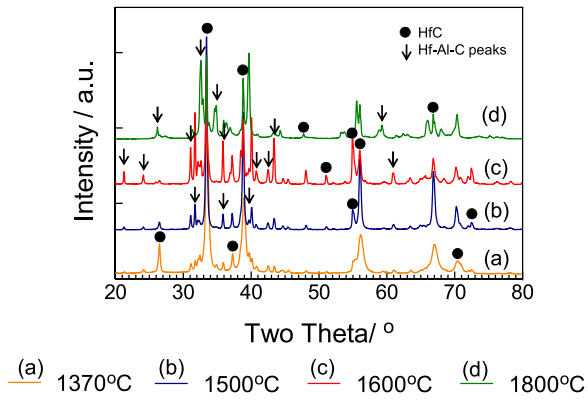

Fig. 3. XRD pattern of Hf-Al-C sample sintered at 1370 °C, 1500 °C, 1600 °C and 1800 °C; applied pressure - 20 MPa and holding time - zero min; • peaks matched HfC (ICDD 039-1491).

be applied in the SPS equipment used in this study. In addition, interrupted studies from lower temperatures were performed in the SPS to determine the microstructural evolution leading to $Hf_2Al_4C_5$. The first trial was carried out at 1370 °C with no holding time. The compact was taken out from the graphite die and powder X-ray Diffraction (XRD) analysis was carried out from the crushed pellet.

Phase analysis was conducted by XRD (PANalytical XRD; Almelo, The Netherlands) using Cu Kα radiation with signals collected at 0.03 ° steps. Diffraction peaks were indexed using ICDD (International Centre for Diffraction Data) cards #039-1491 for HfC and #059-312 for $Hf_2Al_4C_5$. Lattice parameter (a) was measured at each peak and plotted against cos2θ; data points were fitted using the least squares method and line was extrapolated to the axis where cos2θ = 0 (y-intercept). Samples for scanning electron microscopy (SEM) were mounted in epoxy resin and polished in successive steps using diamond composite discs and slurries. Microstructural analysis was performed using an SEM (Auriga, Carl Zeiss; Oberkochen, Germany) operated in backscattered electron (BSE) and secondary electron (SE) imaging modes at an accelerating voltage of 15 kV. Elemental analysis was conducted using an ultra-thin window Energy Dispersive Spectroscopy (EDS) unit (X-Max 20, Oxford instruments; Abingdon, UK). Transmission electron microscopy (TEM) was conducted using a JEOL FX2100 (Tokyo, Japan) and elemental analysis by EDS (X-Max 80, Oxford instruments; Abingdon, UK). Samples of 3 mm diameter were cut from sintered bulk, ground and polished to 30 μm thickness using a disc grinder, dimpled using a dimple grinder (Gatan 656 Dimple Grinder, Abingdon, UK) with 1 μm paste to a <10 μm thickness and ion-polished using a Precision Ion Polishing System (PIPS, Gatan 691, AMETEK (GB) Limited, Leicester, UK) to electron transparency. Samples were analysed at 200 kV and with bright-field (BF) image and dark-field (DF) image formation plus SAED (Selected Area Electron Diffraction) in STEM (Scanning Transmission Electron Microscopy) mode. Fast Fourier Transforms (FFT) were taken from the images using the DigitalMicrograph software package. SAED patterns were indexed using single crystal diffraction patterns from Williams and Carter [12] and TEM diffraction analysis software (SingleCrystal, CrystalMaker Software Ltd.; Begbroke, UK).

Thermal diffusivity ($D_{thermal}$) was measured by the laser flash technique (LFA-427 Netzsch, Germany) from room temperature to 1573 K in high purity argon gas for samples of 10 mm diameter and 3 mm thickness. A laser pulse (450 V for 0.8 ms) was shot into the sample front face and the temperature was detected from the rear face using an IR detector. Three measurements were taken at each temperature and the average value of the thermal diffusivity is plotted versus the temperature. Specific heat capacity (C_p) values were taken from previously cited work from room temperature to 1523 K in air. Thermal conductivity (k) was calculated using the following relationship:

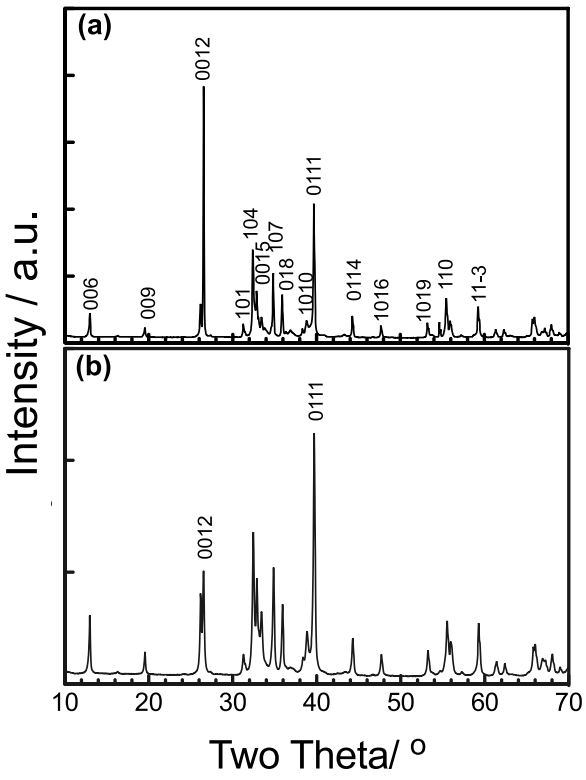

Fig. 4. XRD pattern of Hf-Al-C sample sintered at 1900 °C, (a) SPS (20 MPa/20 min) and (b) HP(30 MPa/60 min). All peaks matched $Hf_2Al_4C_5$ (ICDD 059-312).

$$k_\alpha = D_{thermal}.\rho.C_p \quad (1)$$

Oxidation studies were carried out for the hot-pressed samples for 3 h at 1300 °C in a bottom loading furnace. Phase and microstructural analyses were performed on oxidised samples.

3. Results and discussion

3.1. Phase analysis

Fig. 3(a) shows the XRD pattern of the sample SPS'd at 1370 °C with no holding time. All peaks correspond to HfC although with some traces of other (unidentified) peaks indicating that the reaction between Hf and C occurred well below 1370 °C to form predominantly HfC. However, the temperature is insufficient for formation of any Hf-Al-C phases. Fig. 3(b) shows XRD of the sample SPS'd at 1500 °C with no holding time and with a minimum pressure of 20 MPa. Although, HfC peaks become narrow and well defined indicating high crystallinity, other peaks also arise. The peaks indicated by arrows are newly formed but unidentified Hf-Al-C phase. Fig. 3(c) and (d) show XRD from samples SPS'd at 1600 °C and 1800 °C, respectively. The intensity of HfC peaks start to decrease with increasing temperature and they were significantly reduced at 1800 °C with Hf-Al-C peaks becoming predominant thereafter.

Hf-Al-C compositions were also sintered using the hot press and Fig. 4 shows XRD from Hf-Al-C samples hot-pressed for 3 h at 1900 °C. All peaks correspond to the $Hf_2Al_4C_5$ ternary carbide in the Hf-Al-C system and the peaks were indexed according to ICDD data (ICDD 059-312). The lattice parameters (a = 3.308 Å and c = 40.832 Å) of this phase were calculated and the c/a ratio value (12.343) is in reasonable agreement with the value obtained by He et al. [21], where c/a ratio = 12.3083. Fig. 4 compares XRD of Hf-Al-C samples sintered by SPS (Fig. 4 (a), 1900 °C, 20 MPa, 20 min) and HP (Fig. 4(b), 1900 °C, 30 MPa, 3 h). The XRD patterns indicate the completion of $Hf_2Al_4C_5$ formation with no trace of unreacted HfC or other phases. The $Hf_2Al_4C_5$ crystallized with

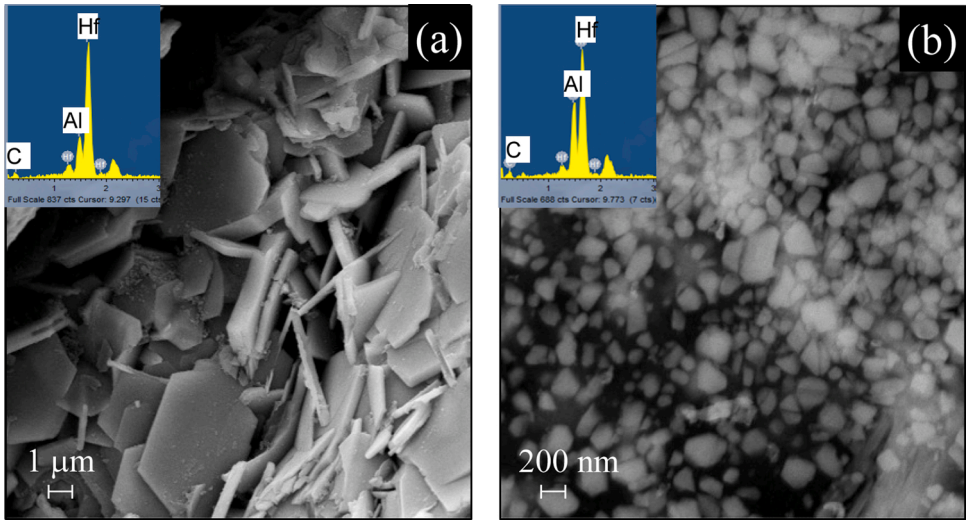

Fig. 5. Microstructures of $Hf_2Al_4C_5$ sintered at 1600 °C using SPS technique. (a) platelet morphology of grains (less than 10 µm in size, with thickness from 0.3–0.6 µm) inside a pore and (b) clusters of sub-micron (< 200 nm) sized particles on the surface.

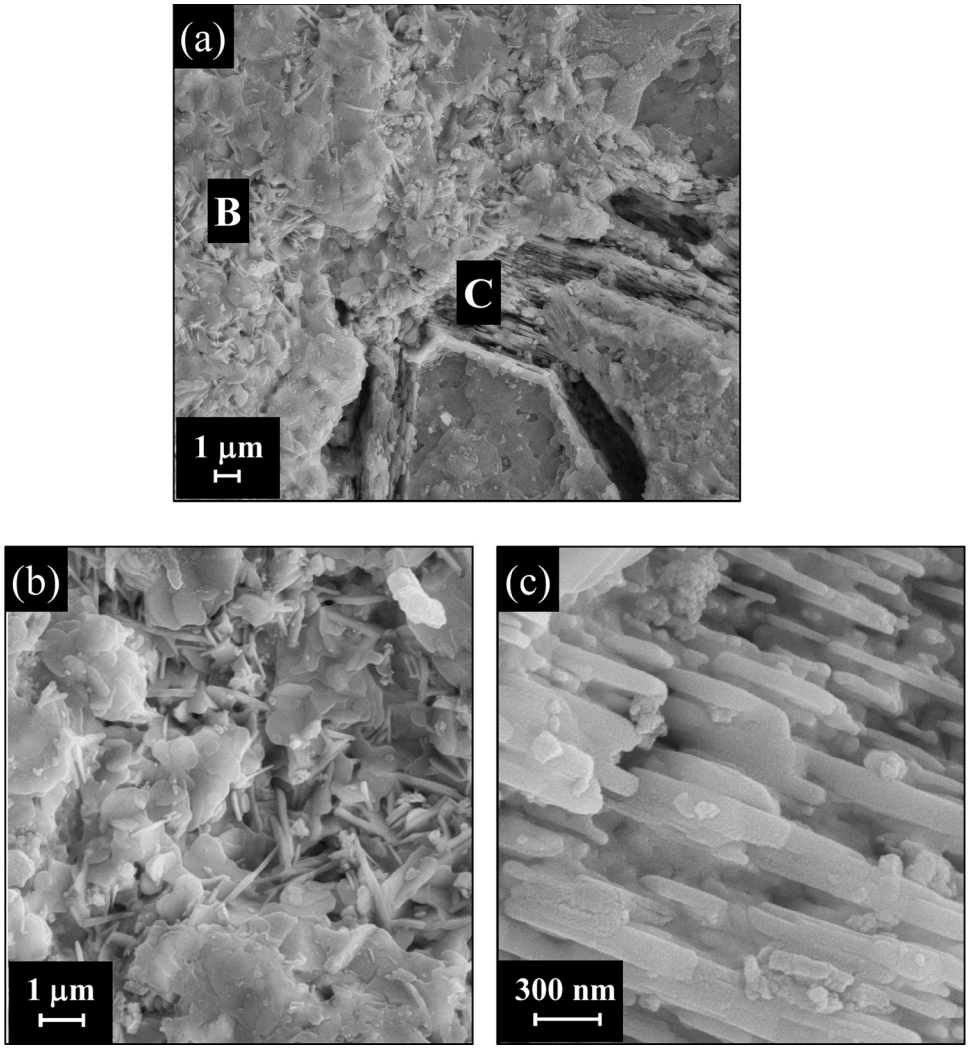

Fig. 6. (a) Microstructures of $Hf_2Al_4C_5$ sintered at 1800 °C using SPS technique, (b) higher magnification of region 'B' labelled in Fig. 6(a) and (c) higher magnification of region 'C' labelled in Fig. 6(a).

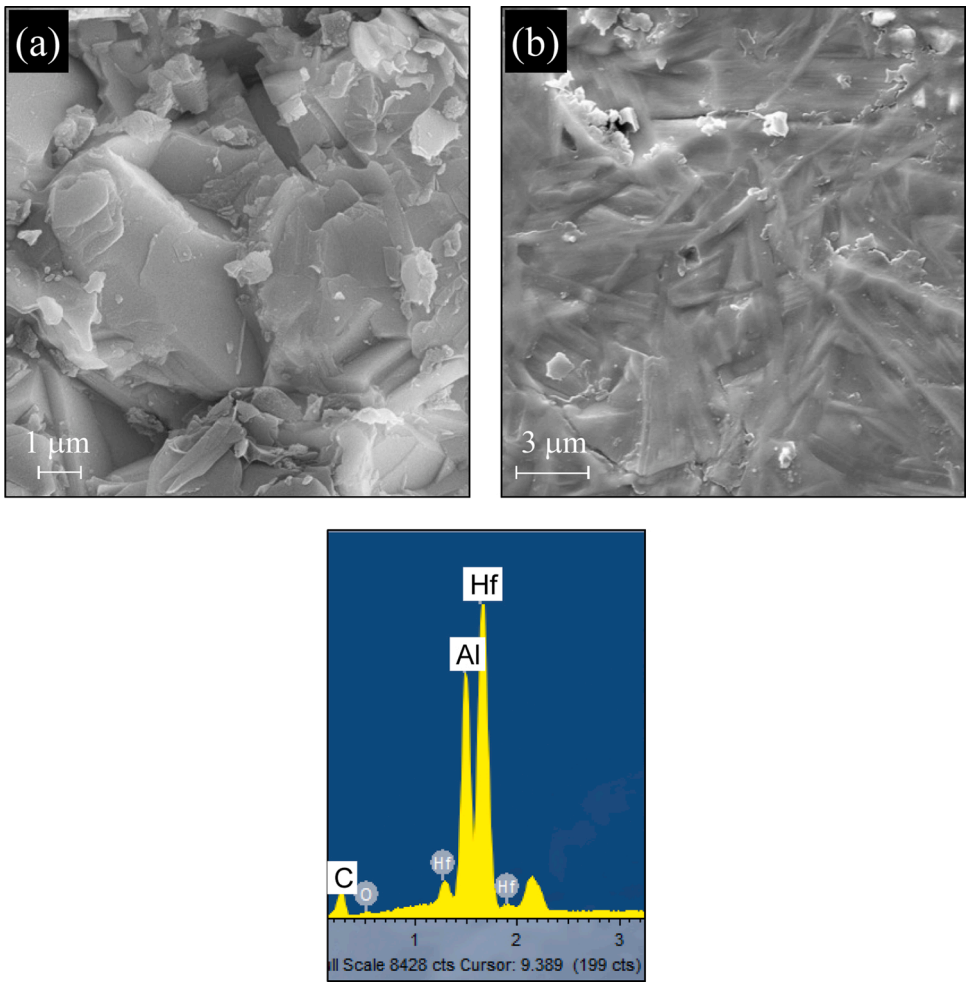

Fig. 7. Microstructures of $Hf_2Al_4C_5$ sintered at 1900 °C using HP technique. (a) Fracture surface and (b) polished surface.

rhombohedral symmetry with a space group of *R*3m. The difference in the intensities of 0012 and 0111 peaks between the two XRD patterns indicates the texturing of grains. These XRD results suggest that the intermediate HfC formed in the early stage of sintering may affect $Hf_2Al_4C_5$ formation.

3.2. Microstructural analysis

Fig. 5(a) shows the morphology of $Hf_2Al_4C_5$ grains observed inside a pore/pit on the surface of the sample after SPS'ing at 1600 °C with no holding time. These hexagonal plate-like grains are less than 10 μm in size, with thickness from 0.3–0.6 μm. All platelets exhibit a smooth surface, indicating that they grow and develop from liquid or vapour. The EDS shown as insert confirms the presence of Hf, Al and C. Another typical feature observed on the surface in the same sample is clusters of sub-micron (< 200 nm) sized particles shown in Fig. 5(b). EDS area analysis (inset in Fig. 5(b)) of these small angular particles shows the region contains Hf, Al and C but with higher Al than in $Hf_2Al_4C_5$. The grains might be HfC surrounded by dark Al-rich phase or they might be Hf-Al-C grains. Point analysis might have contained interference from neighbouring phases. The microstructures of $Hf_2Al_4C_5$ samples SPS'd wth no hold at 1800 °C (Fig. 6(a)) reveal different features. Regions B and C in Fig. 6(a) are shown at higher magnification in Fig. 6(b) and (c). Region B contains needles and platelets while region C contains elongated rod or lath like grains. The $Hf_2Al_4C_5$ grain texturing suggested by XRD in Fig. 3 can be evidently seen in Figs. 4 and 5. It can be suggested that the liquid phase owing to the melting of the phases during the synthesis favours the formation of elongated grains and they were grown from liquid through nucleation and growth mechanism. The 10 μm long and ~ 0.2 μm diameter rod-like grains cluster together densely and grow in a single direction with rounded tips. Fig. 7(a) and (b) show the fracture and polished surfaces, respectively of $Hf_2Al_4C_5$ sample hot pressed for 3 h at 1900 °C. Both fracture and sintered surfaces show dense microstructure. They revealed anisometric morphology of grains. The EDS analysis shows the presence of Hf, Al and C.

These observations suggest that Al tends to dissolve in HfC forming a metastable solid solution (Hf,Al)C. The "freely grown" $Hf_2Al_4C_5$ nanocrystals correspond to the early stages of growth of bulk single crystals. In general, the growth morphology of a crystal is determined by the relative growth rates of all possible faces, i.e., the faces with the lowest growth rate will determine the morphology. Previous results show that lower growth rates along *c* than along *a* axis is general for the MAX phases, and the reason why bulk MAX phases often yield grains with a plate-like appearance [25,26,28]. Likely reaction pathways for the formation of $Hf_2Al_4C_5$ are shown below.

$$Al_{sol.} \rightarrow Al_{liq.}\ (\sim 660.3^{\circ}C) \quad (2)$$

$$Hf + C \rightarrow HfC\ (\sim 1300^{\circ}C) \quad (3)$$

$$Hf + Al \rightarrow Hf - Al\ (\sim 1000^{\circ}C) \quad (4)$$

$$(Hf - Al) + HfC \rightarrow Hf - Al - C\ (\sim 1600^{\circ}C) \quad (5)$$

$$HfC + Al \rightarrow Hf - Al - C\ (\sim 1600^{\circ}C) \quad (6)$$

A conceptual reaction pathway and growth mechanism for formation

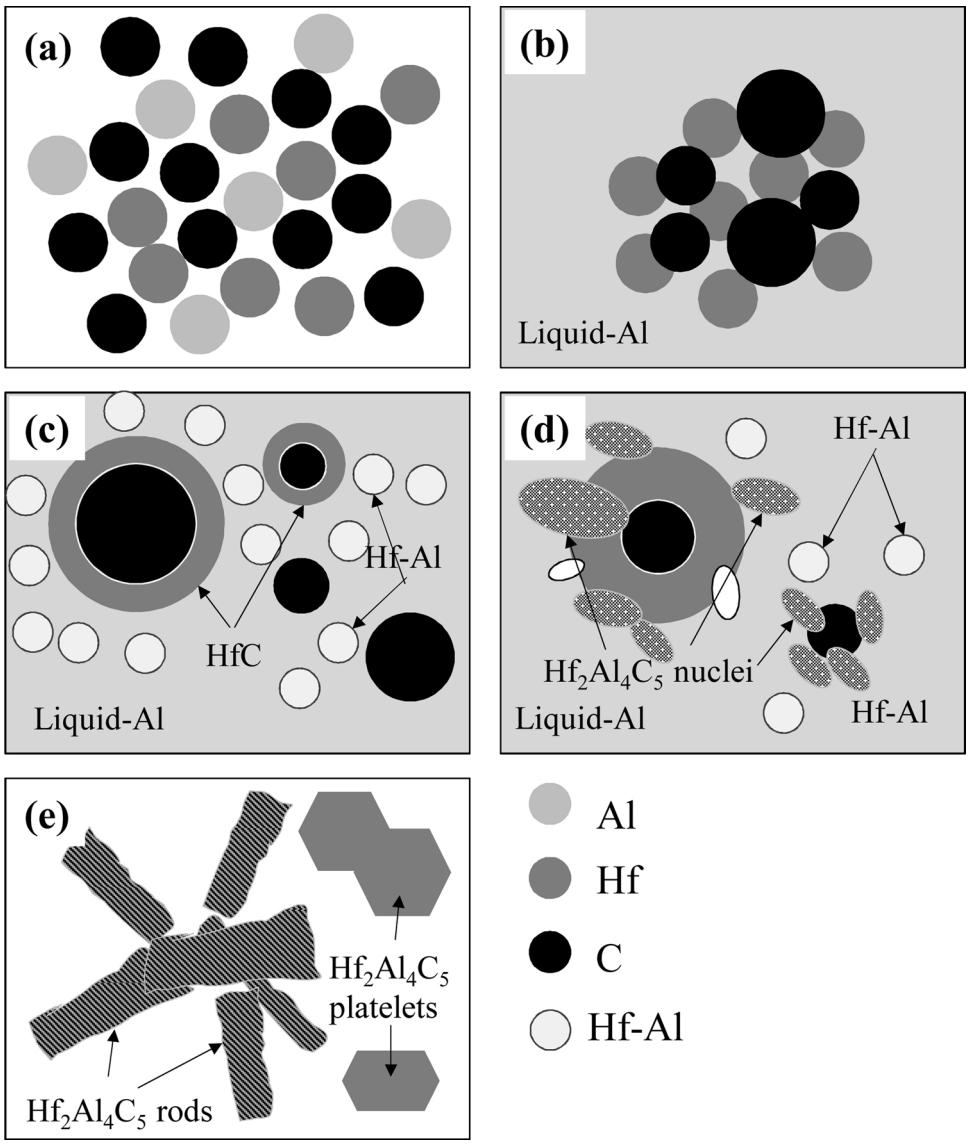

Fig. 8. Conceptual reaction pathway and growth mechanism for the formation of $Hf_2Al_4C_5$ with a bimodal microstructures shown in Figs. 5 and 6. (a) Mixing of starting materials Hf, Al and C, (b) Re-arrangement of Hf and C grains in the presence of liquid Al, (c) Formation of Hf-C and Hf-Al phases, (d) Nucleation and precipitation of $Hf_2Al_4C_5$ and (e) Growth of $Hf_2Al_4C_5$ platelets and rods.

of $Hf_2Al_4C_5$ with a bimodal microstructure [29] is shown in Fig. 8. Initially, powders of Hf, Al and C are mixed homogeneously (Fig. 8(a)). As the temperature increases to above the melting point of Al (~ 660.3 °C), Al starts to melt according to reaction (2). With increasing temperature, molten Al spreads everywhere by capillary action; under this environment, Hf and C particles are easily rearranged and are close to each other (Fig. 8(b)). Hf atoms diffuse toward and accumulate in the grain boundaries of C resulting in formation a thin Hf-C layer (not HfC) owing to the strong chemical affinity of Hf to C (Fig. 8(c)). When the temperature increases to 1000 °C and above, Hf starts to react with Al to form Hf-Al intermetallics (Fig. 8(c)) through reaction 4 [30]. However, XRD analysis did not pick up any of the formed intermetallic phases. On increasing the temperature, the reaction producing $Hf_2Al_4C_5$ takes place between the HfC and Hf-Al compounds observed in the XRD patterns in Figs. 3 and 4. Nuclei of $Hf_2Al_4C_5$ precipitate and grow on the surface of the HfC layer. All the above reactions are exothermic and may occur in the liquid-Al system, in which $Hf_2Al_4C_5$ grows fast and develops on the HfC layer (Fig. 8(d)). With repetition of the above reactions, the smaller C particles are rapidly consumed and nuclei of $Hf_2Al_4C_5$ develop into hexagonal platelets and rods (Fig. 8(e)).

Fig. 9 shows bright-field TEM images of $Hf_2Al_4C_5$ HP sintered 1 h at 1900 °C. A low magnification image of $Hf_2Al_4C_5$ showing different grains is shown in Fig. 9(a). Two different types of grain can be seen: large, elongated grains with high aspect ratio (>10) and sub-micron particles (~50 nm). This bimodal grain size is analogous to the microstructure observed using SEM. Fig. 9(b) shows the STEM image of the interface between labelled regions B and D in Fig. 9(a) at a higher magnification. The large, elongated grains (A, D & E) contain striations typical of polytypic layered structure ceramics such as SiC. Fig. 9(c) is the high magnification BF image in another region showing layered structure. Fig. 7(d) is the SAED pattern taken along [110] direction taken on the elongated grain of Fig. 9c; the streaks are indicative of faults in the stacking sequence of the layered structure. Fig. 9(e) is a high magnification BF image of elongated grains in another region having layered structure and exhibiting a high density of stacking faults. Previous work by Wang et al. [11] demonstrated that the mismatch and strain energy between hexagonal HfC and Al_4C_3 were small; so that formation of layered ternary carbides in Hf-Al-C system was possible. Song et al. [27], observed two types of stacking faults were observed and characterized inside $Hf_2Al_4C_5$ grains — the major one with additional

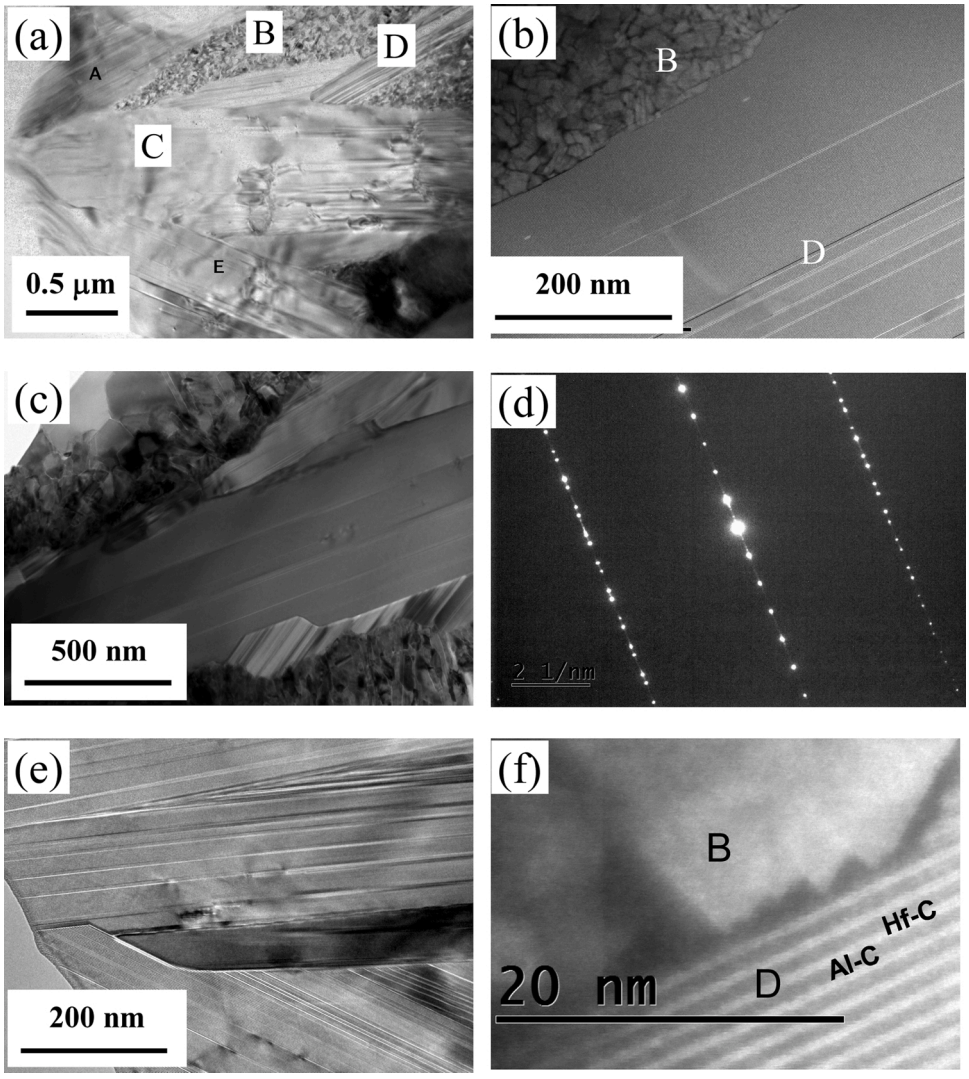

Fig. 9. TEM images of $Hf_2Al_4C_5$ ceramic reactive sintered at 1900 °C by hot press technique. (a) BF image, (b) STEM image, (c) high magnification BF image, (d) SAED pattern taken along z.a. [110] on the elongated grain in Fig. 9(c), (e) high magnification BF image of elongated grains with striations and (f) high magnification STEM image of the interface of grains B and D shown in Fig. 9(a).

insertion of Al_4C_3 units, and the minor one with additional insertion of HfC units. Both of these stacking faults result from the competitive growth of HfC and Al_4C_3 slabs. It is observed in this study that two major factors might play important roles during stacking fault formation: one is growth faults produced during *in-situ* synthesis of Hf–Al–C compounds using Hf, Al, and graphite as starting materials; the other is "stress-induced" stacking faults formed during hot-pressing or on cooling and result from residual thermal stresses due to the anisotropy in the thermal expansion coefficients along the *c* and *a* axes. Fig. 9(f) shows a high magnification STEM image of the interface region between small grains and large grain, B and D labelled in Fig. 9(b), respectively. In large grain, dark and bright slabs can clearly be seen. EDS analysis carried out in the STEM mode confirmed that the dark slab contains Al and C, and bright slab contains Hf and C. Careful observation of the two different contrast slabs in the STEM image in Fig. 9(f), reveals the dark slab (Al-C) is slightly thicker than the Hf-C slab, consistent with the layers in the $Hf_2Al_4C_5$ crystal (Fig. 1).

Fig. 10 shows a detailed HRTEM microstructural analysis. Fig. 10(a) shows a region containing small crystals and enlarged grains. The box containing labelled grains of B and C is shown in Fig. 10(b). The SAED pattern (Fig. 10(b)) taken on large grains along the zone axis [110] confirms it as a super layer structure. Fig. 10(c) and (d) show the interfaces of regions between B|C and C|bottom grain, respectively. The HRTEM image reveals the layered structure of the grains [27]. Both HRTEM images show that the grain boundaries are free of amorphous phase. This is beneficial to the high temperature mechanical properties of Hf-Al-C ceramics. The reason why there is no grain boundary glass phase in Hf-Al-C ceramics lies in the fact that no sintering additive was uses when using elemental powders as starting materials; moreover, carbon in the form of graphite flake acts as a reducing agent for oxides at high temperatures. Further, although liquid Al is involved in the reaction pathway in the formation of the ternary carbide, at the high sintering temperatures used in this study, Al evaporates and leaves behind liquid free interface.

Fig. 11 shows the high resolution TEM image of $Hf_2Al_4C_5$ ceramics obtained with the incident beam parallel to the [110] direction and Fig. 11(b) shows the SAED taken along the zone axis [110] and the diffraction points are indexed. The enlarged image of the square marked in Fig. 11(a) is shown in Fig. 11(c) and the corresponding FFT filtered image is shown Fig. 11(d). The inset shows the simulated pattern of $Hf_2Al_4C_5$ crystal using crystal maker. The simulated pattern can be easily super imposed with FFT filtered image. The enlarge image of simulated pattern of $Hf_2Al_4C_5$ crystal can be seen in Fig. 11(e). The dark layer is Hf-C and the bright layer is Al-C. It is very clear from the

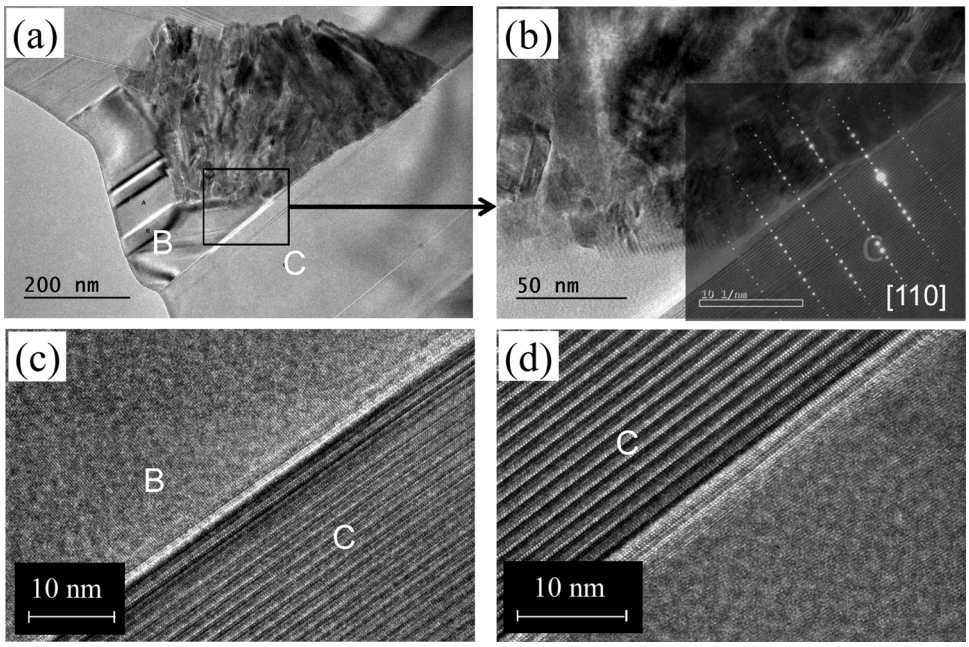

Fig. 10. HRTEM images of $Hf_2Al_4C_5$ ceramic reactive sintered at 1900◦C by hot press technique. (a) A region containing small crystals and enlarged grains; (b) High magnification of the boxed region in Fig. 10(a) and corresponding SAED taken along the z.a [110]; (c) HRTEM image showing the interface between grains B and C in Fig. 10(a) and (d) the interface showing the other side of grain C in Fig. 10(a).

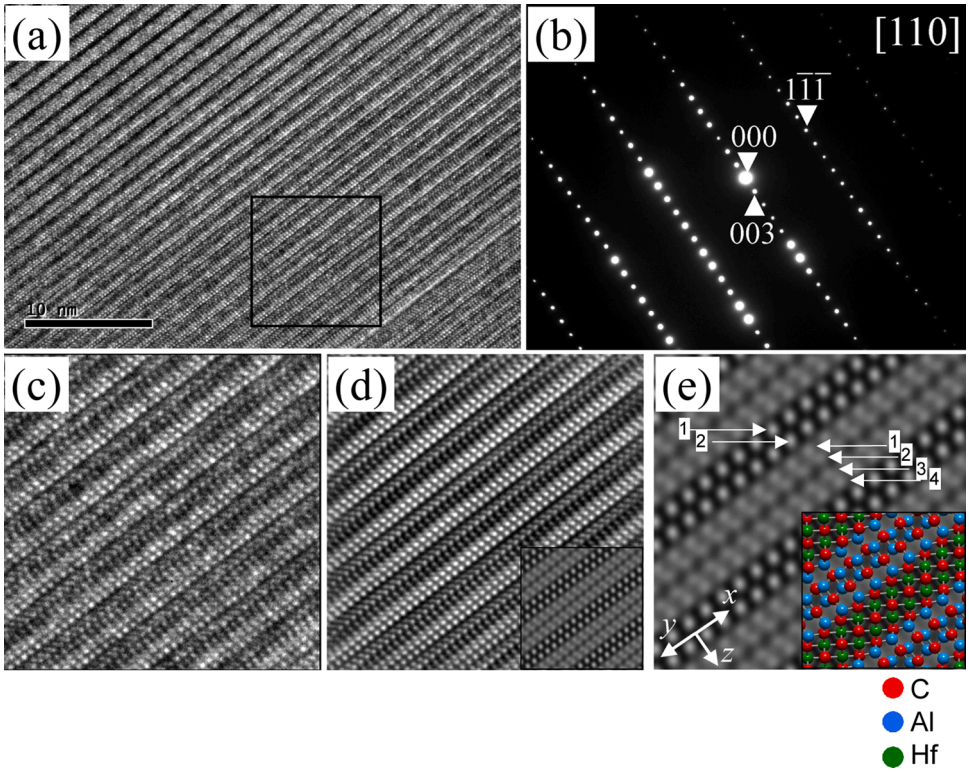

Fig. 11. (a) and (c) HRTEM images of $Hf_2Al_4C_5$ ceramic reactive sintered at 1900◦C by hot press technique, (b) SAED taken along the [110] zone axis of the grain, (d) FFT image of (a) and (e) simulated pattern of. $Hf_2Al_4C_5$ crystal using crystal maker and the insert is the crystal structure of $Hf_2Al_4C_5$.

simulated pattern, which is perfectly aligned with FFT filtered image that two Hf-C slabs are separated by an Al_4C_3 layer. The arrows in Fig. 11 (e) indicate the arrangement of atoms in $Hf_2Al_4C_5$ revealing two Hf-C layers in one Hf-C slab and 4 Al-C layers. The atomistic model shown in the inset of Fig. 9(e) is created by crystal maker. The lattice parameters calculated from the FFT filtered image of Fig. 8(d) are a = b = 3.082 Å, c = 38.30 Å, α=β = 90 °, γ = 120 ° which are in good agreement with the lattice parameters calculated from XRD measurements. This clearly proves that the ternary carbide obtained is $Hf_2Al_4C_5$.

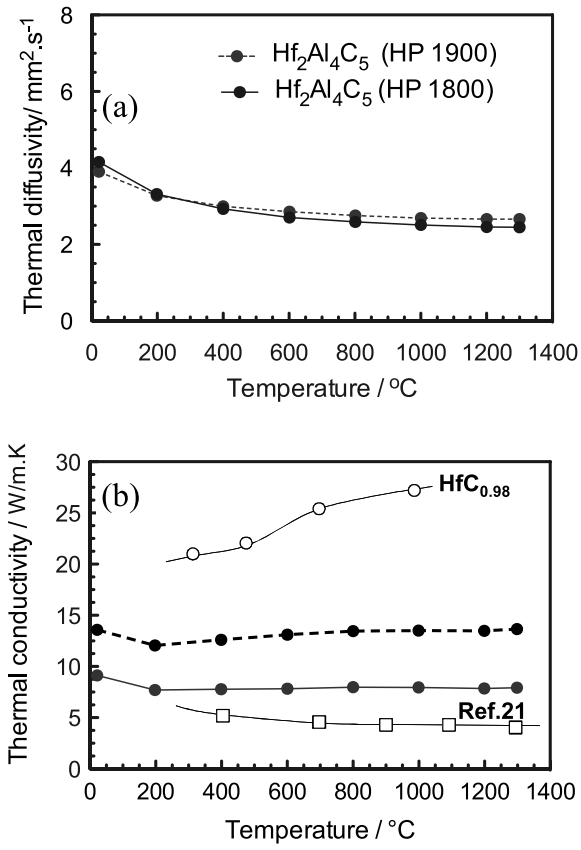

Fig. 12. (a) Thermal diffusivity and (b) thermal conductivity of $Hf_2Al_4C_5$ ceramics hot pressed at 1900 °C for 3 h.

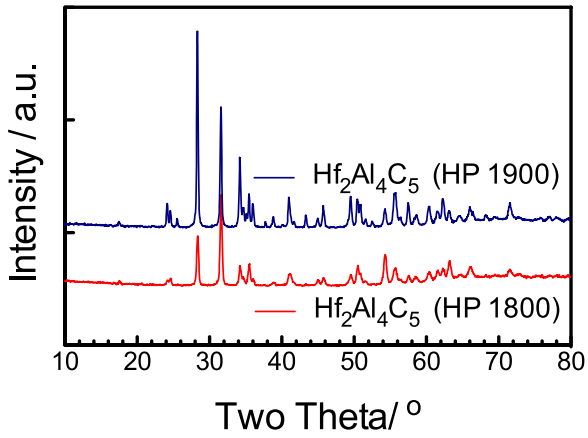

Fig. 13. XRD pattern of $Hf_2Al_4C_5$ sample oxidised for 1 h at 1300 °C.

3.3. Thermal properties

Thermal diffusivity and thermal conductivity of $Hf_2Al_4C_5$ ceramics hot pressed 3 h at 1900 °C are shown in Fig. 12(a) and (b), respectively. Thermal diffusivity initially decreases first and then plateaus with increase in temperature to 1300 °C. However, thermal conductivity of both samples either increased feebly or remain unchanged with an increase in temperature (14 W/m.K for hot pressed sample at 1900 °C, and 9 W/m.K for hot pressed sample at 1900 °C). $Hf_2Al_4C_5$ has relative lower stiffness and higher electrical resistivity than HfC, which results in its low phonon and electron contribution of thermal conductivity [21]. Therefore, $Hf_2Al_4C_5$ has a lower thermal conductivity than HfC. However, over the whole temperature range, the thermal conductivity of

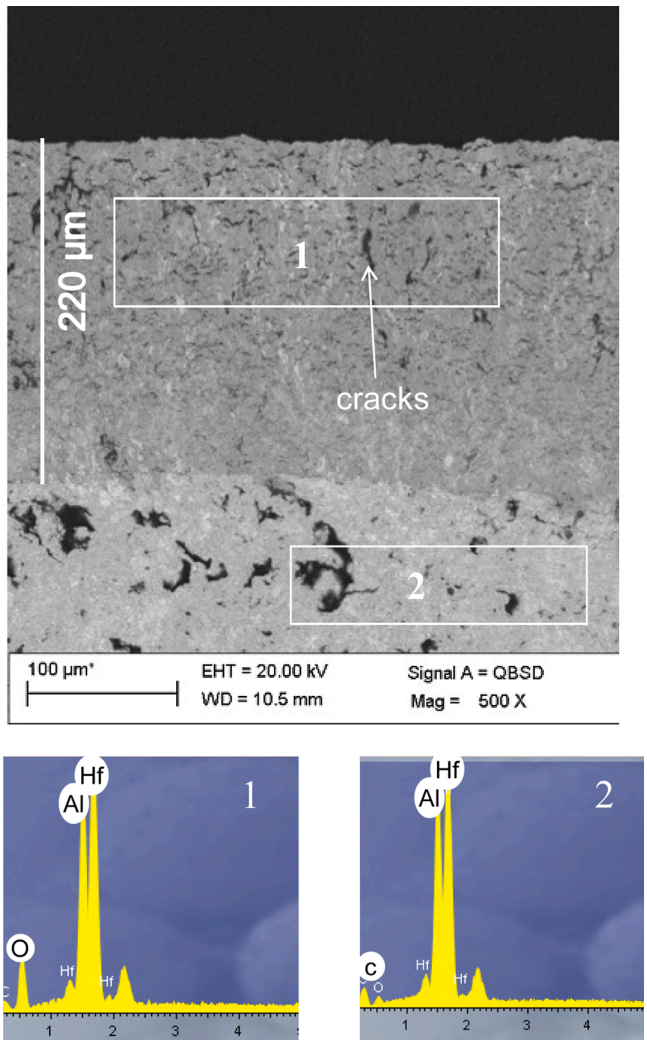

Fig. 14. Cross-section microstructures of hot-pressed $Hf_2Al_4C_5$ oxidised for 3 h at 1300 °C.

$Hf_2Al_4C_5$ is still higher than the values obtained by He et al. for Hf-Al-C composite. They suggested the reason for their low values is that their Hf–Al–C composite contained more defects, especially carbon vacancies. The main difference is, the ceramics fabricated in this study is single phase $Hf_2Al_4C_5$ whereas the samples fabricated by He et al. are $Hf_2Al_4C_5$ containing composites.

3.4. Oxidation studies

XRD of $Hf_2Al_4C_5$ samples oxidised for 3 h at 1300 °C in air is shown in Fig. 13. The pattern at the bottom corresponds to the sample hot pressed for 3 h at 1800 °C whereas that on the top corresponds to the sample hot pressed 3 h at 1900 °C. The oxidised surfaces of both samples reveal identical phases present on the surface, which are *m*-HfO_2 and Al_2O_3. The oxidation of HfC under low oxygen partial pressure could produce equivalent amounts of HfO_2 and carbon. Similarly, it is possible to form carbon, HfO_2 and Al_2O_3 simultaneously under low oxygen partial pressure during oxidation of $Hf_2Al_4C_5$. The low oxygen partial pressure is caused by the formation of HfO_2 and Al_2O_3 scales, which act as an oxygen diffusion barrier and likely contributes to a significant decrease in the oxygen activity at the scale/substrate interface. The cross-section microstructure of the HP (1900 °C) $Hf_2Al_4C_5$ sample oxidised for 3 h at 1300 °C is shown in Fig. 14. The oxidation layer thickness is around 220 µm and it contains many microcracks closer to the sample top whereas the interface between the $Hf_2Al_4C_5$ and the oxidized layer

looks seamless without any crack or spallation of oxide layers. EDS analysis carried out on the top layer in box 1 shows Hf, Al and O suggesting the presence of HfO_2 and Al_2O_3 phases on top. Three comments can be made on the oxide scales. First, high-speed diffusion of O_2, CO, and CO_2 at high temperatures may break up the scales and make them porous and cracked. Second, oxidation of the remaining carbon will leave microchannels between the oxide grain boundaries, which may be the source of the cracking. Third, the porous and loose scale is also related to the poor sinterability of formed oxides at low temperatures. However, the scale of $Hf_2Al_4C_5$ ceramics still shows fewer cracks and better bonding with the substrate. EDS analysis taken on box 2 in the substrate reveals Hf, Al and C and trace of O.

4. Conclusion

Single-phase $Hf_2Al_4C_5$ ceramics have been obtained from Hf/Al/C powder mixtures by reaction sintering using SPS and HP techniques. $Hf_2Al_4C_5$ with a bimodal microstructure of plate-like and rod-like grains appeared in the samples after sintering. A possible reaction pathway and growth mechanism for the formation of $Hf_2Al_4C_5$ has been suggested. The evolution of $Hf_2Al_4C_5$ formation involved with the melting of all starting materials and precipitation of nuclei, which resulted in a final microstructure of hexagonal platelets (10 μm in size, with thickness from 0.3–0.6 μm) and elongated (10 μm long and ~ 0.2 μm diameter) laths along with (200 nm) crystal. Liquid Al played an important role in the formation of stoichiometric $Hf_2Al_4C_5$ ceramics. Al tends to dissolve in HfC forming a metastable solid solution (Hf,Al)C. All of the above reactions are exothermic and may occur in the liquid-Al system, in which $Hf_2Al_4C_5$ grows fast and develops on the HfC layer. It is evident from HRTEM analysis that two Hf-C layers were sandwiched with 4 Al-C layers (Al_4C_3) in the $Hf_2Al_4C_5$ ternary carbide.

Data availability

Data will be made available on request.

Declaration of Competing Interest

The authors declare that they have no known competing financial interests or personal relationships that could have appeared to influence the work reported in this paper.

Acknowledgement

The author DD would like to thank Imperial College London and Kingston University for providing the support.

References

[1] M.M. Opeka, I.G. Talmy, E.J. Wuchina, J.A. Zaykoski, S.J. Causey, Mechanical, thermal, and oxidation properties of refractory hafnium and zirconium compounds, J. Europ. Ceram. Soc. 19 (1999) 2405–2414.
[2] K. Upadhya, J.M. Yang, W.P. Hoffman, Materials for ultra high temperature structural applications, Am. Ceram. Soc. Bull. 76 (1997) 51–57.
[3] D. Sciti, M. Nygren, Spark plasma sintering of ultra refractory compounds, J. Mater. Sci. 43 (2008) 6414–6421.
[4] C.B. Bargeron, C.R. Benson, A.N. Jette, T.E. Phillips, Oxidation of hafnium carbide in the temperature range 1400° to 2000°C, J. Am. Ceram. Soc. 76 (1993).
[5] S. Kang, Some issues in Ti(CN)-WC-TaC cermets, Mater. Sci. Eng. A 209 (1996) 306–312.
[6] S.S. Ordanyan, G.P. Zaitsev, A.M. Khokhlov, M.I. Sokhor, Sintering and homogenization in HfC - TaC system, J. Appl. Chem. USSR 50 (1977) 1392–1397.
[7] H.F. Jackson, D.D. Jayaseelan, D. Manara, C.P. Casoni, W.E. Lee, Laser melting of zirconium carbide: determination of phase transitions in refractory ceramic systems, J. Am. Ceram. Soc. 94 (2011) 3561–3569.
[8] H.F. Jackson, D.D. Jayaseelan, W.E. Lee, M.J. Reece, F. Inam, D. Manara, C. P. Casoni, F. De Bruycker, K. Boboridis, Laser melting of spark plasma-sintered zirconium carbide: thermophysical properties of a generation IV very high-temperature reactor material, Int. J. Appl. Ceram. Technol. 7 (2009) 316–326.
[9] A. Paul, D.D. Jayaseelan, S. Venugopal, E. Zapata-Solvas, J. Binner, B. Vaidhyanathan, A. Heaton, P. Brown, W.E. Lee, UHTC composites for hypersonic applications, Bull. Am. Ceramic Soc. 91 (2011) 22–29B.
[10] W.E. Lee, R. Harrison, E. Giorgi, A. Maitre, O. Rapaud, Nuclear applications for ultra-high temperature ceramics and MAX phases, chapter 15, in: W. G. Fahrenholtz, E.J. Wuchina, W.E. Lee, Y. Zhou (Eds.), Ultra-High Temperature Ceramics: Materials for Extreme Environment Applications, Wiley, 2014, pp. 391–415.
[11] J. Wang, Y. Zhou, Recent progress in theoretical prediction, preparation, and characterization of layered ternary transition-metal carbides, Annu. Rev. Mater. Res. 39 (2009) 415–443.
[12] Y. Zou, Z. Sun, S. Tada, H. Hashimoto, Effect of Al addition on low-temperature synthesis of Ti_3SiC_2 powder, J. Alloys Compd. 461 (2008) 579–584.
[13] J. Zhu, Effect of aluminum on the reaction synthesis of ternary carbide Ti3SiC2, Scr. Mater. 49 (2003) 693–697.
[14] W.B. Zhou, B.C. Mei, J.Q. Zhu, Fabrication of high-purity ternary carbide Ti_3SiC_2 by spark plasma sintering technique, Mater. Lett. 59 (2005) 1547–1551.
[15] M.W. Barsoum, The $M_{N+1}AX_N$ phases: A new class of solids: Thermodynamically stable nanolaminates, Progress in Solid State Chemistry 28 (2000) 201–281.
[16] C. Hu, F. Li, J. Zhang, J. Wang, J. Wang, Y. Zhou, Nb_4AlC_3: a new compound belonging to the MAX phases, Scr. Mater. 57 (2007) 893–896.
[17] Z.M. Sun, Progress in research and development on MAX phases: a family of layered ternary compounds, Int. Mater. Rev. 56 (2011) 143–166.
[18] D. Horlait, S. Grasso, N. Al Nasiri, P.A. Burr, W.E. Lee, Synthesis and oxidation testing of MAX phases in the Cr-Ti-Al-C quaternary system, J. Am. Ceram. Soc. 99 (2016) 682–690.
[19] D. Horlait, S. Grasso, A. Chroneos, W.E. Lee, Attempts to synthesise quaternary MAX phases $(Zr,M)_2AlC$ and $Zr_2(Al,A)C$ as a way to approach Zr_2AlC, Mater. Res. Lett. 4 (3) (2016) 137–144.
[20] Y.-C. Zhou, L.-F. He, Z.-J. Lin, J.-Y. Wang, Synthesis and structure–property relationships of a new family of layered carbides in Zr-Al(Si)-C and Hf-Al(Si)-C systems, J. Eur. Ceram. Soc. 33 (2013) 2831–2865.
[21] Z.J. Lin, M.J. Zhuo, L.F. He, Y.C. Zhou, M.S. Li, J.Y. Wang, Atomic-scale microstructures of Zr2Al3C4 and Zr3Al3C5 ceramics, Acta Mater. 54 (2006) 3843–3851.
[22] L. He, Z. Lin, J. Wang, Y. Bao, M. Li, Y. Zhou, Synthesis and characterization of bulk Zr2Al3C4Ceramic, J. Am. Ceram. Soc. 90 (2007) 3687–3689.
[23] L.F. He, Z.J. Lin, J.Y. Wang, Y.W. Bao, Y.C. Zhou, Crystal structure and theoretical elastic property of two new ternary ceramics Hf3Al4C6 and Hf2Al4C5, Scr. Mater. 58 (2008) 679–682.
[24] L.F. He, Y.W. Bao, J.Y. Wang, M.S. Li, Y.C. Zhou, Microstructure and mechanical and thermal properties of ternary carbides in Hf–Al–C system, Acta Mater. 57 (2009) 2765–2774.
[25] C.I. Michaenko, Y.B. Kuz'ma, V.E. Popov, V.N. Gurin, A.P. Naetshitaylov, A. N. Nardov. 4th Conference on the Crystal Chemistry of Intermetallic Compounds, 1978.
[26] H. Nowotny, J.C. Schuster, P. Rogl, Structural chemistry of complex carbides and related compounds, J. Solid State Chem. 44 (1982).
[27] K. Song, H. Zhang, K. Du, D. Qi1, H. Chen, X. Wang, Jian-Feng Nie, H. Ye, Atomic-scale microstructure of $Hf_2Al_4C_5$ ceramic synthesized by spark plasma sintering, J. Am. Ceram. Soc. 00 (2017) 3208–3216.
[28] N.F. Gao, Y. Miyamoto, D. Zhang, Dense Ti_3SiC_2 prepared by reactive HIP, J. Mater. Sci. 34 (18) (1999) 4385–4392.
[29] Shi-Bo Li, Guo-Ping Bei, Hong-Xiang Zhai, Yang Zhou, Bimodal microstructure and reaction mechanism of Ti_2SnC synthesized by a high temperature reaction using Ti/Sn/C and Ti/Sn/TiC powder compacts, J. Am. Ceram. Soc. 89 (12) (2006) 3617–3623.
[30] Y.C. Zhou, H.Y. Dong, B.H. Yu, Development of two-dimensional titanium tin carbide (Ti_2SnC) plates based on the electronic structure investigation, Mater. Res. Innov. 4 (2000) 36–41.